Detection of cardiac-induced motion in murine cerebrospinal fluid space captured in vivo with synchrotron radiation-based microtomography

Mattia Humbel[a], Marta Girona Alarcón[b], Willy Kuo[b], Irene Spera[c], Britta Bausch[b], Luca Fardin*[d], Hans Deyhle[a], Griffin Rodgers[a], Britta Engelhardt[c], Steven Proulx[c], Vartan Kurtcuoglu[b], Bert Müller[a], and Christine Tanner*[a]

[a]Biomaterials Science Center, Department of Biomedical Engineering, University of Basel, 4123 Allschwil, Switzerland
[b]The Interface Group, Institute of Physiology, University of Zurich, 8057 Zurich, Switzerland
[c]Theodor Kocher Institute, University of Bern, 3012 Bern, Switzerland
[d]European Synchrotron Radiation Facility, 38043 Grenoble, France

ABSTRACT

Transport of immune cells, nutrients and waste products via the cerebrospinal fluid (CSF) has been implicated in the development of neurological disorders. Using time-resolved *in vivo* microtomography, we investigated pulsatile motion of CSF spaces in the mouse brain as a potential driver of CSF flow. Here we present a method for detecting motion captured in murine brain images acquired *in vivo* at the European Synchrotron Radiation Facility. Anesthetized mice were placed in a heated holder that was designed to minimize head motion and maintain physiological body temperature. Contrast agent was infused into the ventricle to improve visibility of the CSF spaces. Projections were retrospectively sorted based on the ECG recording. Cardiac phase images were reconstructed in 10 ms intervals from the ECG peak and automatically analyzed for decorrelation. Motion was automatically quantified by non-rigid registration. Regions with high intensity structures, large motion magnitudes, large improvements in image similarity due to registration, or at the contrast-enhanced ventricles were visually inspected for structures with motion artifacts prior to registration. We detected mainly motion in the nasopharynx, skin, ear channels, and bones in the range of 2.3 to 14.8 µm magnitude. Small motion artifacts were detectable only for high-contrast structures. No misalignments were visible for the contrast-enhanced ventricles at a voxel resolution of 6.30-6.45 µm. In the future, dedicated active gating to ensure regular sampling and local scans with improved spatial resolution will be used to investigate the limits to the detection of *in vivo* ventricular motion in mice.

Keywords: Cerebrospinal fluid dynamics, Ventricular motion, In vivo imaging, Image registration, X-ray virtual histology

1. INTRODUCTION

The cerebrospinal fluid (CSF) is a liquid surrounding the central nervous system (CNS) involved in maintaining CNS homeostasis, e.g. through transport of immune cells, nutrients and waste products.[1,2] Disturbance of CSF flow is associated with neurological disorders such as Alzheimer's disease[3] and multiple sclerosis.[4] Pulsatile behavior of CSF flow caused by cardiovascular and respiratory action has been established via phase contrast magnetic resonance imaging in humans.[5,6] However, applying these techniques in mice is challenging due to lower nominal velocities, higher heart and respiratory rates, smaller CSF space sizes requiring higher spatial resolution and the need for anesthesia.[7] As experiments in mouse models of disease are indispensible for the development and safety testing of new therapeutic drugs, a different technique is required.

*Luca Fardin is now at the Department of Medical Physics and Biomedical Engineering, University College London, London WC1E 6BT, United Kingdom. Send correspondence to Christine Tanner, e-mail: christine.tanner@unibas.ch, Telephone: +41 61 207 54 34, www.bmc.unibas.ch.

Developments in X-Ray Tomography XV, edited by Bert Müller, Ge Wang,
Proc. of SPIE Vol. 13152, 1315214 · © 2024 SPIE
0277-786X · doi: 10.1117/12.3028460

In this study, we employ *in vivo* synchrotron radiation-based microtomography with contrast enhancement of the ventricular space to assess oscillatory expansion and contraction of brain ventricular space induced by pulsating arterial blood flow as a potential driver of pulsatile CSF flow in mice. Respiratory and cardiac gated microtomography for *in vivo* imaging of mice has been proposed for cardiopulmonary structures[8] and lungs.[9] Recently, gated 4D microtomography acquisitions with impressive spatial and temporal resolutions have been achieved for oscillating *ex vivo* materials,[10] e.g. for excised human middle ears stimulated at 128 Hz and imaged with a voxel size of 2.75 µm.[11] It remains to be seen how the proposed guidelines[10] can be applied to quasi-periodic motion and are compatible with radiation dose restrictions for *in vivo* imaging.

The motion of the ventricles is expected to be relatively small, i.e. a few voxels compared to the image resolution. On the other hand, the 4D dataset is relatively large, e.g. 4.6×10^9 voxels per mouse, height level and cardiac phase image. Thus, motion detection by visual inspection is labor intensive and potentially incomplete. Therefore, we developed a method to semi-automatically detect motion in sequences of phase images.

2. MATERIALS AND METHODS

2.1 Materials

The study involved six wild type C57BL/6J mice aged approximately 12 weeks, housed in a synchrotron facility for a week before experiments. The study followed European animal experimentation guidelines (L358-86/609EEC) and was approved by the French Ministry of Research (APAFIS 30913-2021040211343677v1). Mice received a single dose of buprenorphine (0.1 mg/kg body weight) for analgesia and thirty minutes later an intraperitoneal injection of 73 mg/kg ketamine and 0.18 mg/kg medetomidine to induce anesthesia. Anesthesia depth was monitored and renewed as needed. After imaging, mice were humanely sacrificed under deep anesthesia. Their weights, the respiration state, and the employed contrast agent infusion rates and volumes are stated in Table 1.

2.2 In vivo experimental set-up

The anesthetized mice were prepared for X-ray imaging by applying eye ointment and shaving their skull, neck, and upper thoracic region.

The mice were placed in a mouse stereotactic frame for ventricular cannula insertion for contrast agent infusion. The infusion system consisted of a customized 28G, 2.3 −2.5 mm long PEEK microcannula glued to a fitting tube which was connected to a 25 µL Hamilton syringe without a needle. Before surgery, the syringe and tubing were attached to the syringe pump and filled with mineral oil as a hydraulic fluid, ensuring no air bubbles remained. Next, 2 µL of air were drawn and the tube was glued to the microcannula to prevent liquid mixing. The contrast agent was loaded just before implantation to prevent drying and obstruction. The contrast agent was vortexed for 2 minutes, then 17 µL was drawn and 2 µL expelled into the mannitol solution (54.6 mg/mL in H_2O). A midline skin incision was made to expose the skull, which was thinned with a dental drill. The microcannula was carefully inserted into the right lateral ventricle[12,13] and sealed with cyanoacrylate glue. Tracheotomy was performed for the ventilated animals. We ensured the mice's core temperature was maintained to prevent hypothermia under anesthesia. They were placed in a custom pre-warmed box at 33 °C

Table 1. Overview of weight, respiration state and contrast agent parameters for the six successfully imaged mice.

Mouse ID	Sex	Weight [g]	Respiration state	Contrast agent concentration [mg Ba/mL]	Infusion rate [µL/min]	Infusion volume [µL]
17	male	23.7	free-breathing	240	0.5	5.0
31	female	24.4	ventilated	320	0.5	5.0
46	male	23.6	ventilated	320	1.1	5.0
54	male	25.6	ventilated	320	0.2	2.5
55	male	25.5	ventilated	320	0.2	2.5
56	male	25.5	ventilated	320	0.2	2.5

during anesthesia induction. During surgery, heating pads were used to maintain body temperature at 37 °C. Further details are described in Girona Alarcón et al.[14]

After surgery, the mice were placed in a custom setup consisting of: (1) an additively manufactured mouse holder for temperature control and instrument access; (2) a 200 mm diameter rotating stage for CT projections; and (3) a drag chain to manage cables and sensors during rotation. The mouse holder was made from polyamide 12 and 3D printed with a photopolymer. We positioned mice upright to limit interferences from high density structures like bones and reduce local tomography artifacts. Three-point fixation at each side of the upper skull and a bite bar in a nose cone ensured stability during the experiment. Body temperature regulation was maintained by circulating warm water through the holder using a thermostat pump located in the control room next to the hutch, allowing temperature adjustments without interrupting X-ray acquisition.

During imaging, the remote-controlled syringe pump delivered contrast agent with relatively low infusion rates and small total volumes to maintain the physiological state of CSF, see Table 1. The tracheal cannula was connected to a SAR-1000 ventilator supplied with oxygen-enriched air. The tracheal pressure curve was monitored by a side stream. To implement positive end-expiratory pressure (PEEP), expiratory gases passed through a water column before being expelled into room air. Safety parameters were chosen from the literature: peak inspiratory pressure (PIP) 15 cmH_2O, PEEP 5 cmH_2O, tidal volume 0.35 mL, and respiratory rate 100-120 BPM.[15,16] Inspiration was set to be 35% of the respiratory cycle and was started with the next ECG peak.

We monitored vital parameters using a mouse rectal temperature probe for core body temperature and ECG leads in the front paws and tail for cardiac activity. During beamtime B2 blood oxygenation was measured using a pulse oximeter. Core temperature and when applicable blood oxygenation were continuously tracked with a Physiosuite monitoring device. A data acquisition box synchronously gathered information from the X-ray detector, ECG, and ventilator. It recorded the camera status, ECG signal, ventilator status, and tracheal pressure. Monitoring allowed us to assess changes in anesthesia depth.

2.3 Image acquisition and reconstruction

The images were acquired at the biomedical beamline ID17 of the European Synchrotron Radiation Facility (ESRF, Grenoble, France) during two beamtimes, namely B1 in November 2021 and B2 in June 2022. Monochromatic X-ray energies were 38 keV for B1 and 40 keV for B2. A pco.edge 5.5 sCMOS camera was used to capture the transmitted X-rays. The camera was coupled to a 250 µm thick LuAG scintillator and optics. This configuration resulted in an effective voxel size of 6.30 µm with a FOV of 16.1 mm × 4.9 mm for beamtime B1, and 6.45 µm with a FOV of 16.5 mm × 4.5 mm for beamtime B2.

Gated scans, called phase images, were created retrospectively from subsets of projections acquired at defined time intervals after the peak of the ECG signal as described in Fardin et al.[9] We acquired a total of either 60'000 or 120'000 projections over 360°. The total scan time was either 5 min or 10 min. As many projections as cardiac cycles could then be used to reconstruct each of the 10 ms phase intervals up to the shortest heartbeat duration per time series.

Camera, ECG and respiratory signals were read with the `LabChart` interface (ADInstruments, Dunedin, New Zealand) during beamtime B1 or with `LabVIEW` (National Instruments, Texas, USA) during beamtime B2. The camera signal was zero when the camera was off and otherwise it had a constant value, e.g. 3.34 V. The exact image start signal was not recorded by `LabVIEW` because the camera signal was only sampled with 2 ms and the acquisition time was not exactly 5 ms. Therefore, we determined the most probable true camera signal by simulating undersampled signals and comparing them with the recorded signal, see Fig. 1. Two parameters were optimized, namely the time shift between the true camera-off event and the sampling time, and the time deviation from the expected 5 ms acquisition time. The optimization was performed by grid search. For the `LabChart` data, only the time shift had to be optimized, since the acquisition time could be derived from the detected camera-off events thanks to a sufficient sampling rate. Using `Matlab` (release R2020b; The MathWorks Inc., Natick, USA), the ECG signal was first denoised by discrete wavelet transform via function `imodwt`. ECG peak detection employing the `Matlab` function `findpeaks` was then optimized for minimum peak height (parameter `MinPeakHeight`) and minimum peak separation (parameter `MinPeakDistance`) based on the resulting absolute error to the recorded heart rate.

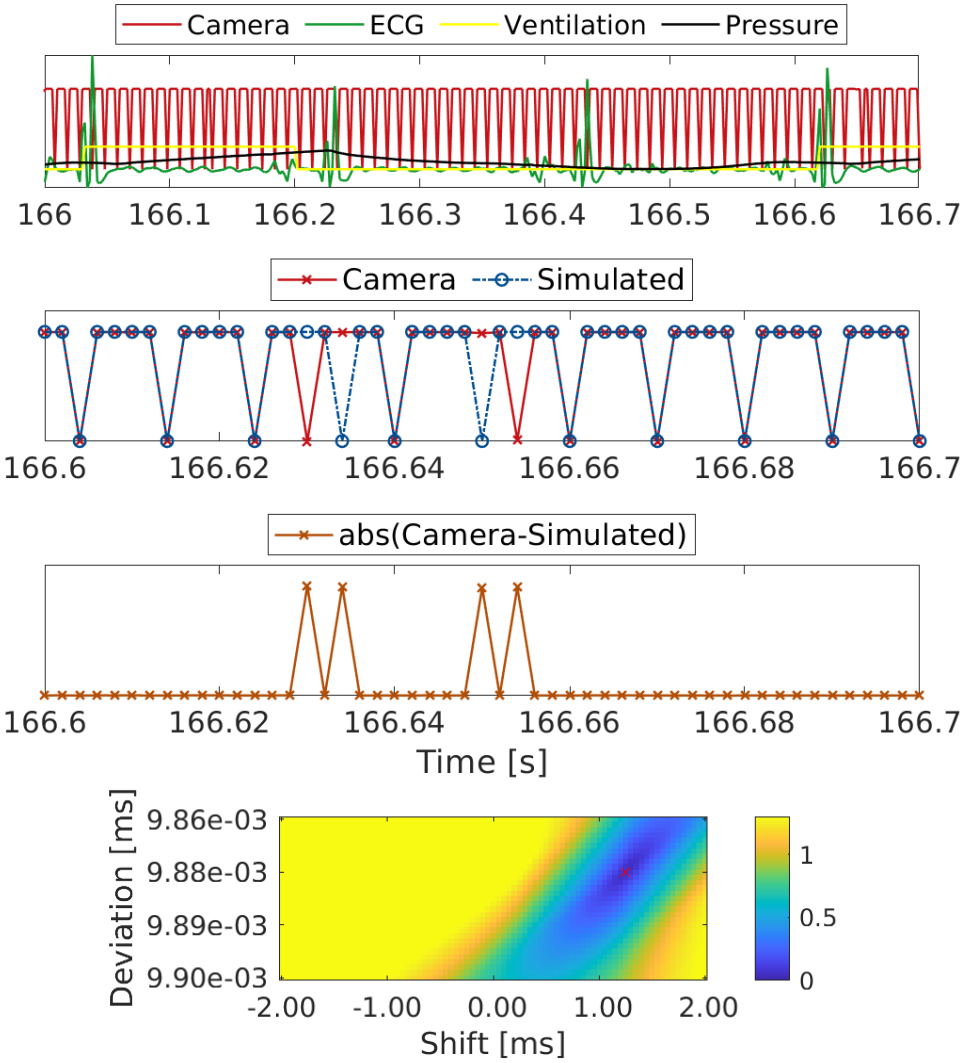

Figure 1. Mouse 56, height level (HL) 3. (Row 1) Example of measured signals for three cardiac cycles during middle part of acquisition showing synchronization of inhale ventilation with ECG peaks. (Row 2) Measured and simulated camera signal for sub-part of Row 1. (Row 3) Absolute difference between measured and simulated camera signal used as error measure for optimization. (Row 4) Result of grid search optimization showing color-encoded mean absolute error with respect to time shift (x-axis) and time deviation from an expected 5 ms acquisition time (y-axis). The lowest error of 0.04 V was marked by a red cross and was achieved for a time shift of 1.25 ms and a time deviation of 9.88 ns.

Image reconstructions were performed based on selecting all projections occurring at a certain time after the ECG peaks, e.g. 10±2.5 ms, with the accepted range automatically set to the acquisition time of one projection. Tomographic reconstructions for Mouse 46, 55, and 56 were performed on ESRF's compute cluster using their nabu software (version 2023.2.0).[17] For Mouse 17 reconstructions were performed in-house, as the raw data was no longer available on the ESRF cluster. They are based on GPU-accelerated filtered backprojection, implemented in the ASTRA Toolbox (version 2.1.0)[18,19] and called from TomoPy (version 1.12.2).[20,21]

2.4 Motion detection and quantification

We calculated the correlation between all possible pairs of cardiac phase images in the region of the skull. The two most decorrelated phase images were then further analyzed for motion quantification.

We used the open source registration software `elastix`[22,23] (version 5.0) to non-rigidly register each of the two most decorrelated phase images (called moving image) to the mean image of the other phases (called fixed image) using normalized correlation coefficient (NCC) as image similarity measure. We determined the amount of regularization by visually inspecting the magnitude image of the displacement fields and the alignment in the difference image after registration for grid spacings of 128, 64 and 32 voxels for one dataset. Specifically, we aimed for the largest regularization which still provided good alignment of image structures. Quantitatively, we compared the relative improvement in the image similarity measure with the relative increase in bending energy.

To detect motion at image structures, we considered three types of image regions of interest (ROIs), namely ROIs centered on (a) large mean absolute difference (MAD) improvements in high intensity regions, (b) large motion magnitudes, and (c) high image intensity values. These ROIs were semi-automatically detected by (1) automatically generating maximum or mean images over the slices of the relevant image (i.e. MAD change, motion magnitude, intensity), (2) visually inspecting these supporting images and manually selecting inplane locations, and (3) automatically determining the image slice with the maximum measure. In addition, every hundredth image slice, from slice 100 to slice 600, was visually inspected for regions showing higher intensities due to contrast agent injection, and the center locations of such ROIs were also selected when applicable. Furthermore, five ROIs were automatically detected based on the best additive ranking with respect to (i) high intensity in the fixed image, (ii) large MAD improvement, and (iii) large motion magnitude. Similarly, another five ROIs were automatically detected based on the best additive ranking of criteria (i) and (ii).

Rectangular regions, centered at the selected locations and with a maximum size of $140\times140\times120$ voxels were extracted. The motion magnitude at the center of a ROI was extracted for the first phase registration and the later phase registration. Statistically significant differences in mean motion magnitude between the first and later phase results from all corresponding ROIs of a dataset were tested at the 0.05 level by paired t-test.

For each region, orthogonal slices of the fixed image, and the difference image before and after registration were visually inspected by one observer, who qualitatively rated the presence of structures and their alignment by answering the following questions:

Does the ROI contain image structures? no ($s_1 = 0$), yes ($s_1 = 1$)
if $s_1 == 1$ **then**
  Are the structures misaligned before registration? no ($s_2 = 0$), a little ($s_2 = 1$), large ($s_2 = 2$)
  How well are the structures aligned after registration?
  much worse ($s_3 = -2$), worse ($s_3 = -1$), same ($s_3 = 0$), better ($s_3 = 1$), much better ($s_3 = 2$)
end if

Only ROIs classified as having misaligned anatomical structures prior to image registration ($s_1 == 1$ and $s_2 > 0$) were further analyzed.

3. RESULTS AND DISCUSSION

3.1 Image acquisition and reconstruction

In vivo distribution of the contrast agent in the ventricles was successfully imaged in four mice. Between one and four height levels (HLs) were acquired per mouse, depending on their vital signs and the time needed for other experiments, see Table 2. Between 1'141 to 1'615 heart beats were observed during the 5 min scans, and between 2'188 and 3'845 heart beats occurred during the 10 min scans. There were as many projections as heart beats available to reconstruct each of the phase images at 10 ms intervals up to the shortest heart beat duration, i.e. 135 ms to 200 ms. We generally reconstructed 10 phases every 10 ms up to 100 ms, as cardiac-induced motion should be greatest shortly after the ECG peak. For Mouse 55 height level (HL) 3, we investigated the usefulness of 5 ms intervals.

Table 2. Overview of *in vivo* contrast-enhanced brain imaging for four mice stating per height level (HL) from left to right: total number of projections, total scan time, average number of heart beats per minute (BPM), range of heart beat duration [ms], number of projections per phase, times after ECG peak of reconstructed phases with s:d:e denoting $\{s, s+d, s+2d, ..., e\}$, and most decorrelated phases. Mouse 17 was acquired during beamtime B1, while all other mice were acquired during beamtime B2.

Mouse ID	HL	Proj. total [#]	Total scan time [min]	Mean heart rate [BPM]	Range beat duration [ms]	Proj. per phase [#]	Reco. phase times [ms]	Most decorr. phases [#]
17	2	60000	10	219.0	[180,330]	2188	10:10:180	1, 15
46	3	60000	5	322.3	[175,195]	1615	10:10:100	1, 10
55	1	120000	10	369.9	[155,170]	3707	10:10:100	1, 9
	2	120000	10	332.6	[135,261]	3330	10:10:100	1, 10
	3	120000	10	324.9	[175,200]	3254	5:5:100	1, 19
	4	120000	10	382.6	[145,195]	3835	10:10:100	1, 9
56	1	60000	5	236.9	[200,416]	1141	10:10:100	1, 10
	2	60000	5	272.1	[190,266]	1355	10:10:100	1, 10
	3	60000	5	286.5	[150,451]	1408	10:10:100	1, 10
	4	60000	5	283.6	[185,245]	1421	10:10:100	1, 10

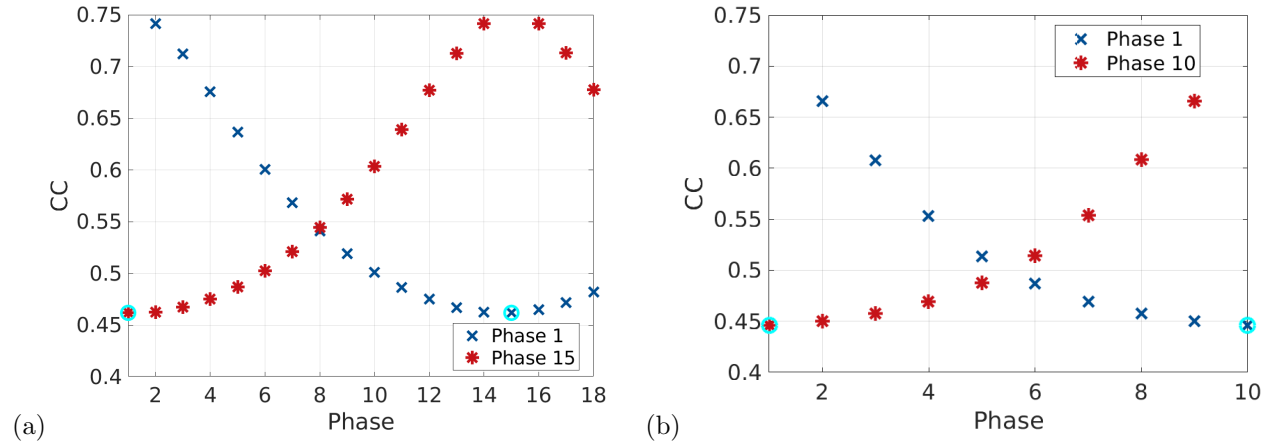

Figure 2. Value of correlation coefficient (CC) between cardiac phase images for the most decorrelated phases of (a) Mouse 17, HL 2 and (b) Mouse 56, HL 3. Lowest values are marked by cyan symbols (o).

3.2 Motion detection and quantification

As the time distance increased, phase images were generally less correlated, see Fig. 2. In 60% of all cases, the two most decorrelated phase images were the first and the last phase, see last column of Table 2. Otherwise it was always the first phase and a late phase (second last or 15th out of 18 phases).

The image similarity measure NCC increased by 0.94%, 1.77%, 1.82% while bending energy increased by 53.6%, 63.6%, 73.0% when the grid spacing was reduced from 256 voxels to 128, 64, 32 voxels, respectively. In view of this, and after visual inspection of the motion magnitude fields and the alignment of local features, see Fig. 3, we decided to use a grid spacing of 64 voxels for non-rigid registration.

Figure 4 shows images supporting the semi-automatic selection of ROIs for Mouse 17. The local improvement in MAD due to non-rigid registration is clearly visible in the nasopharyngeal region and at the anterior skin. Per dataset, we extracted between 12 and 19 ROIs semi-automatically and 10 ROIs automatically. Comparing the motion magnitude between corresponding ROIs, we found that the mean values were statistically significantly larger for the first phase registrations than for the later phase registrations in three out of ten datasets, see Fig. 5. The largest mean motion magnitude was clearly obtained for the first phase registration of Mouse 17 (M17H2).

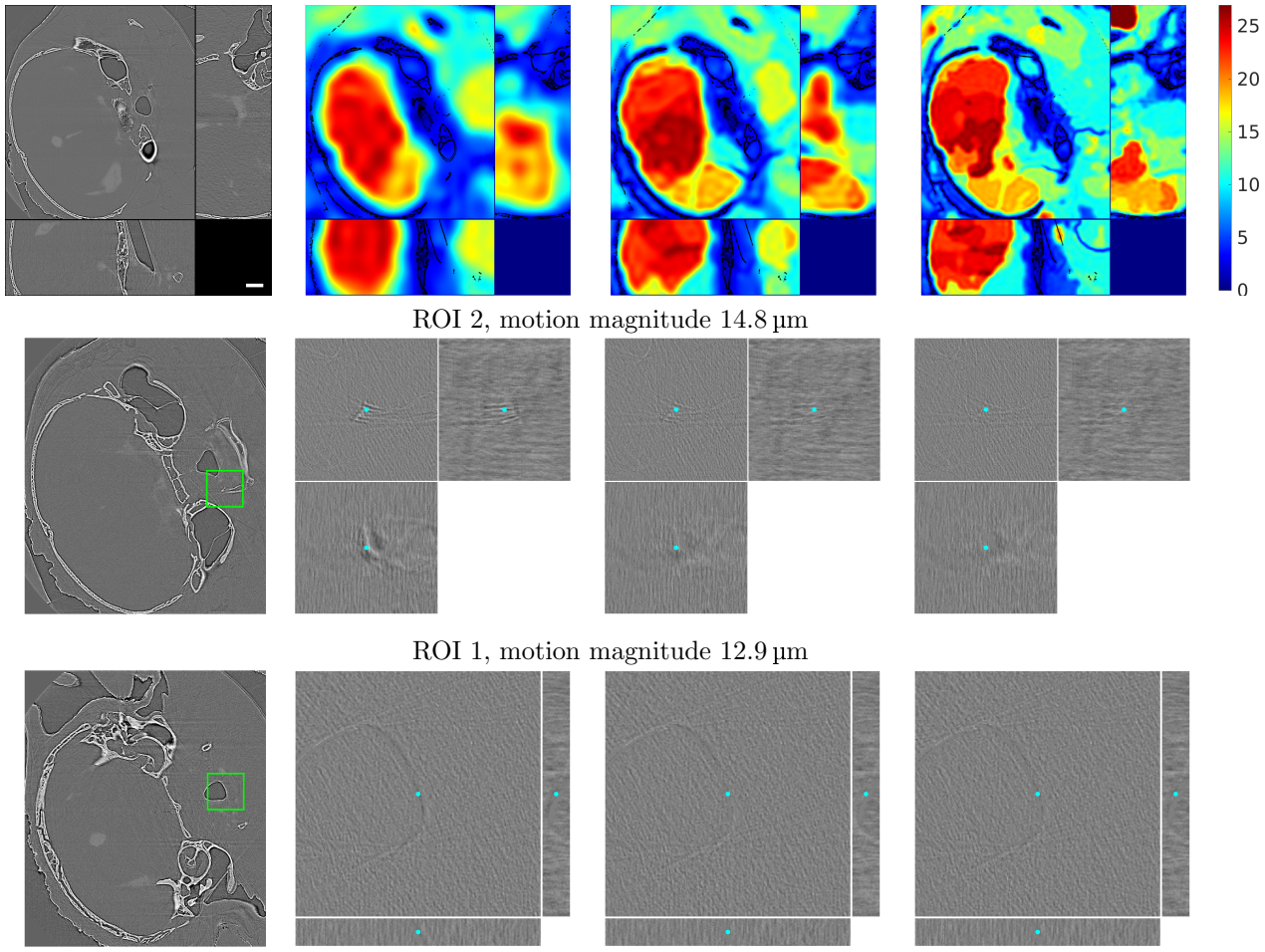

Figure 3. Comparison of non-rigid registration results for Mouse 17, HL 2, phase 1. Row 1: Orthogonal slices of (a) fixed image with 1 mm scale bar and (b-d) motion magnitude images [in µm] after non-rigid registration with (b) 128, (c) 64 and (d) 32 voxels grid spacing. Row 2 and 3: (a) Inplane location of ROI (green rectangle) and (b-d) orthogonal slices of ROIs for difference image after non-rigid registration with (b) 128, (c) 64 and (d) 32 voxels grid spacing. Cyan points show center positions for fixed image and magenta points corresponding position for moving image.

Of the 250 ROIs, only 39 and 3 ROIs, respectively, were classified as containing a misaligned anatomical structure prior to registration for the first phase image and the later phase image, see Table 3.

The detected misalignments were mostly in the nasopharynx, skin, bone, and ear channel. No misalignments were observed in the ventricles, e.g. Fig. 6. Misalignments were judged to be large, i.e. $s_2 == 2$, only for first phase image registrations, namely for the nasopharyngeal region and the anterior skin region of Mouse 17 and for one lateral skin site of Mouse 56. The two regions with the largest motion of structures for Mouse 17 are shown in Figs. 3 and the region with the large motion for Mouse 56 is shown in Fig. 7. The smallest detectable misalignments were at bony structures thanks to high contrast edges, see Fig. 8. Motion patterns for the other three mice are shown Fig. 9. It can be observed that bones have generally very small movements, that motion fields are partitioned and smaller than for Mouse 17. The videos linked to Fig. 10 show the motion between the phase 1 image and the mean image from all other phases for Mouse 17 in the nasopharyngeal region for orthogonal slices and for a rendering of the high intensity structures.

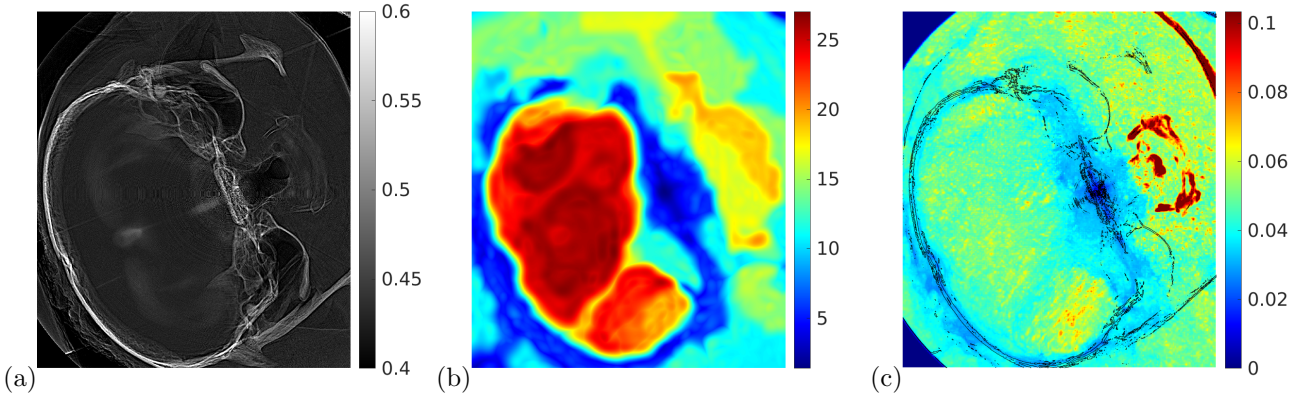

(a) (b) (c)

Figure 4. Images supporting the semi-automatic selection of ROIs for Mouse 17, HL 2, phase 1. (a) Mean intensity over slices for min-max normalized fixed image, (b,c) maximum intensity over slices for (b) motion magnitude [µm] and (c) local improvement in mean absolute intensity difference due to non-rigid registration.

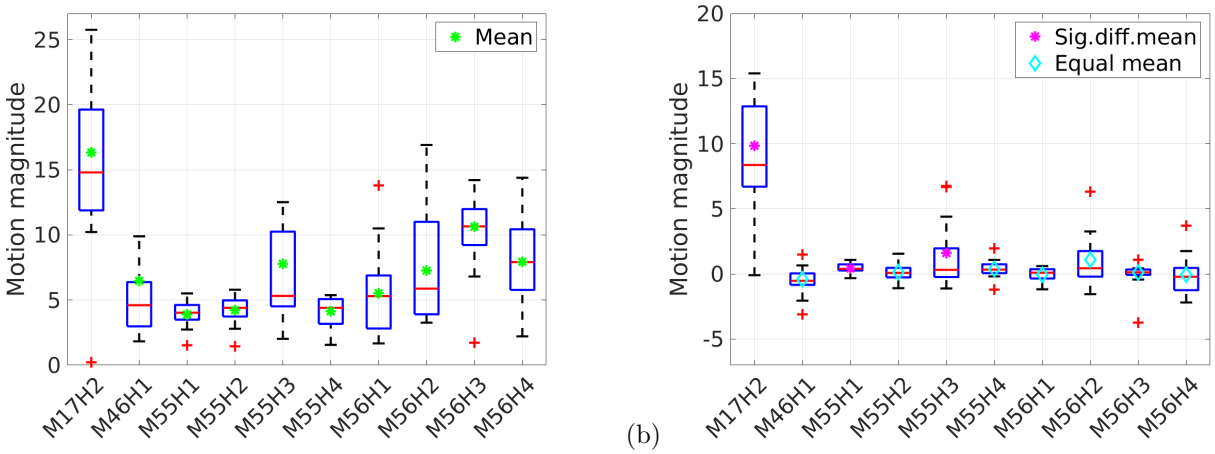

(a) (b)

Figure 5. Boxplots showing distribution of motion magnitude values [µm] for corresponding ROIs after non-rigid registration for the ten datasets (x-axis) of (a) first phase and (b) difference between first phase and later phase with statistically significantly mean differences at the 0.05 level marked by a magenta star (*).

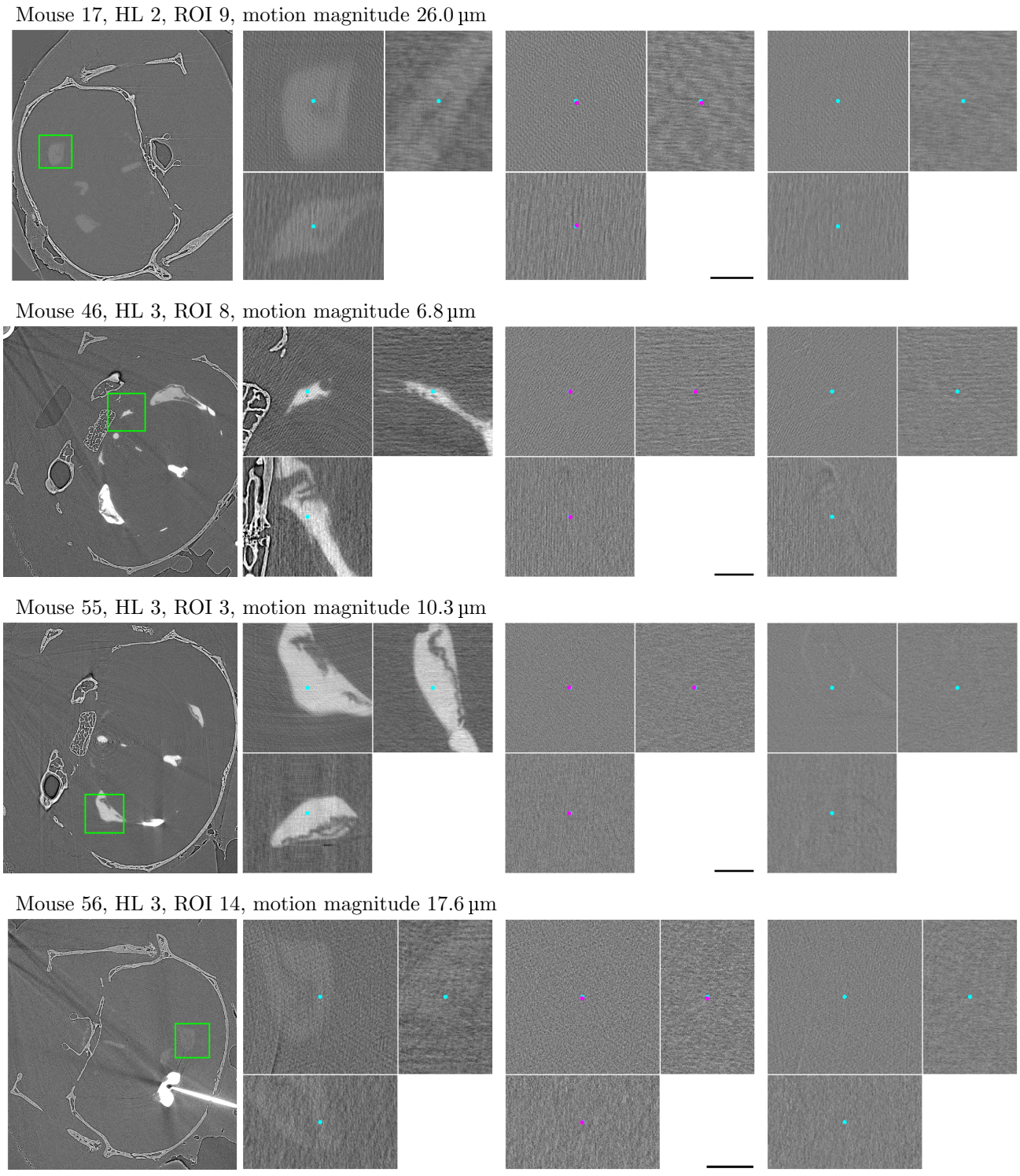

(a) Center plane (b) Fixed image (c) Fixed - moving (d) Fixed - registered

Figure 6. ROIs for contrast-enhanced ventricles with largest motion for (top to bottom) Mouse 17 HL 2, Mouse 46 HL 3, Mouse 55 HL 3, and Mouse 56 HL 3. No misalignment was visible. (a) Center plane with position of ROI marked by green rectangle, (b) mean image without phase 1, (c, d) difference mean image - phase 1 image (c) before registration and (d) after non-rigid registration. Cyan points show the center position for the fixed image and magenta points the corresponding position for the moving image. Scale bars in (c) are 500 µm.

ROI 15, motion magnitude 12.5 µm

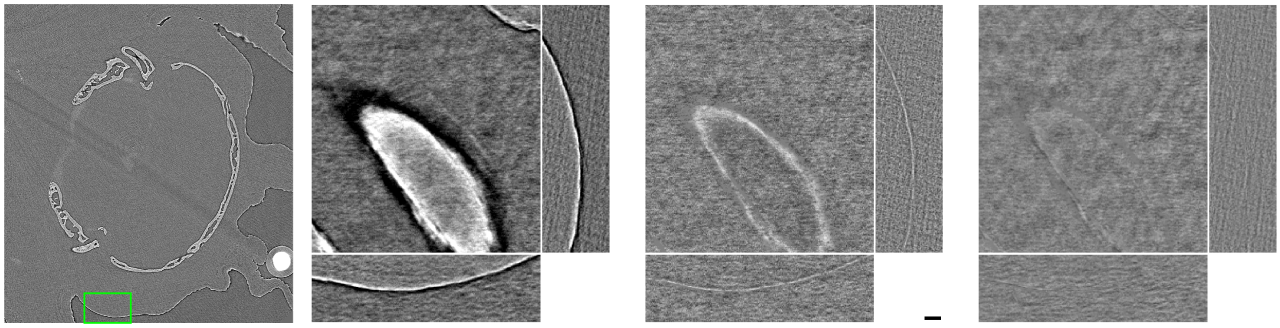

(a) Center plane (b) Fixed image (c) Fixed - moving (d) Fixed - registered

Figure 7. Mouse 56, HL 4, phase 1. ROI with large motion of structures. Meaning of subfigures (a-d) as in Fig. 6. The scale bar in (c) is 100 µm.

ROI 3, motion magnitude 2.3 µm

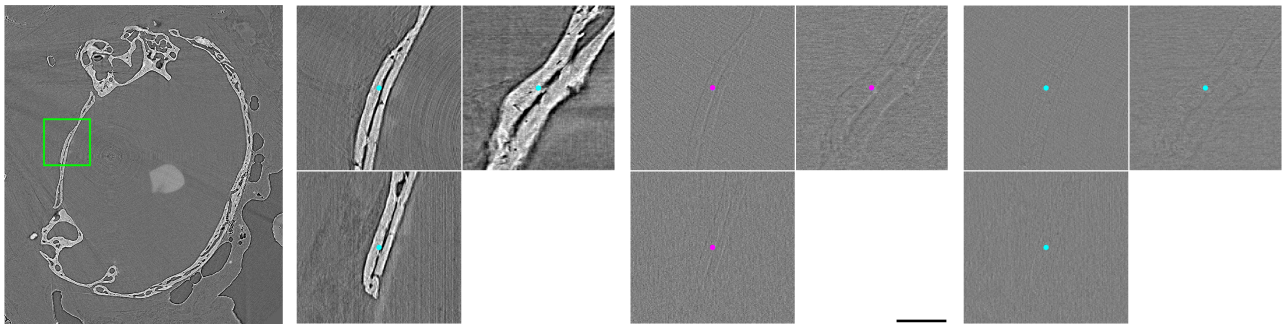

ROI 2, motion magnitude 2.9 µm

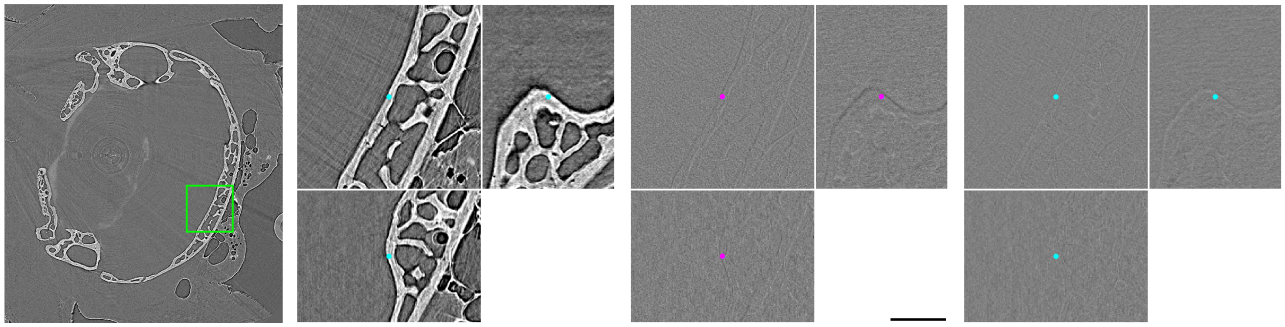

(a) Center plane (b) Fixed image (c) Fixed - moving (d) Fixed - registered

Figure 8. Mouse 55, HL 4, phase 1. ROIs with smallest motion of structures. Meaning of subfigures (a-d) as in Fig. 6.

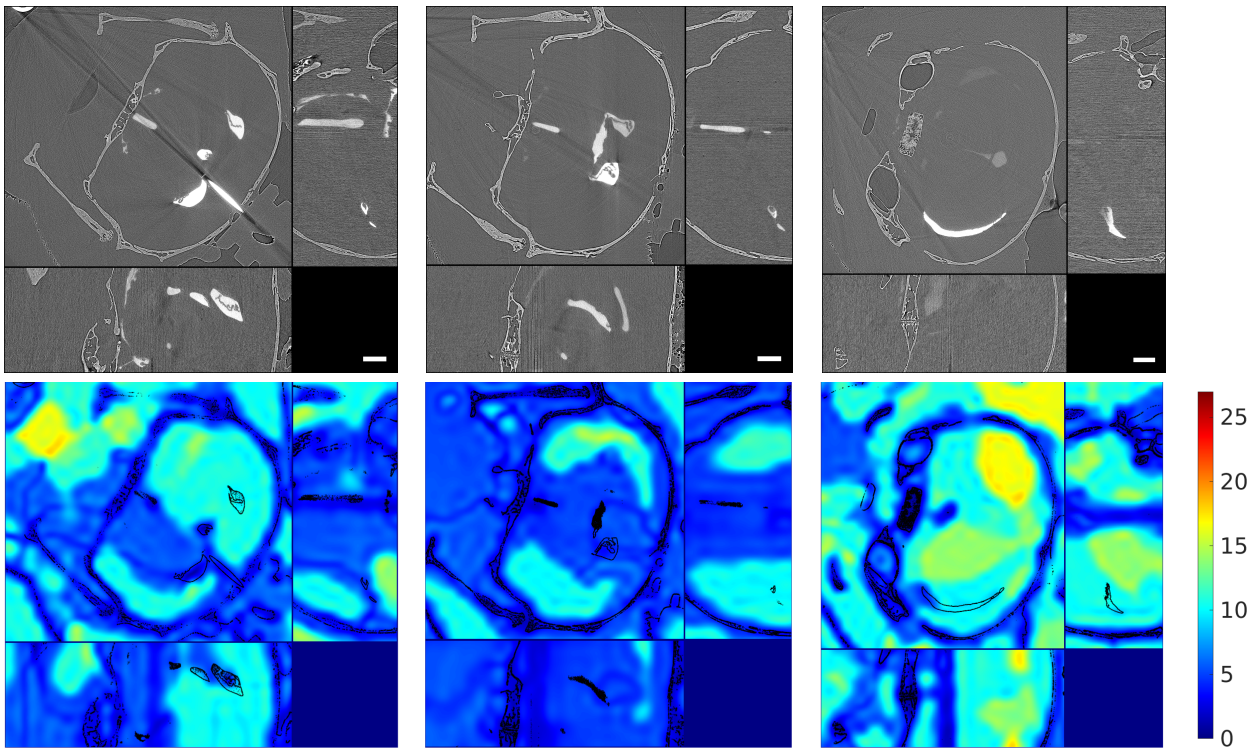

(a) Mouse 46 (b) Mouse 55 (c) Mouse 56

Figure 9. (Top) Orthogonal slices of reconstruction for 10 ms after ECG peak, i.e. phase 1, for (a) Mouse 46 HL 3, (b) Mouse 55 HL 3, and (c) Mouse 56 HL 3. Scale bars are 1 mm. (Bottom) Motion magnitude [µm] from registration of phase 1 image to mean of all other phases with black contours showing high intensity regions.

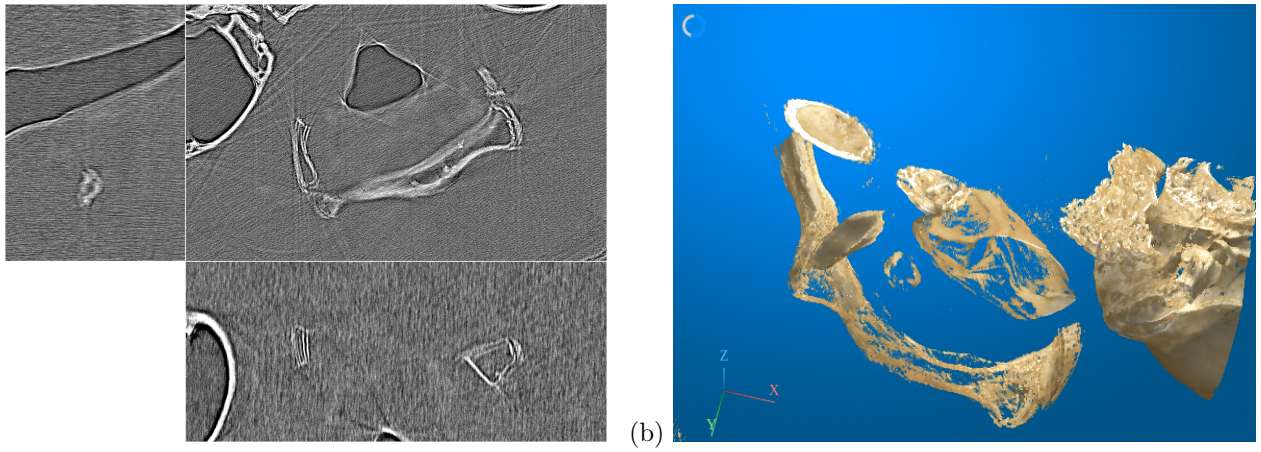

(a) (b)

Figure 10. Mouse 17, HL 2. Motion of 9.9 −14.8 µm between phase 1 and the mean of the other phase images in the nasopharyngeal region. (a) Video 1 shows orthogonal slices. http://dx.doi.org/10.1117/12.3028460.1 (b) Video 2 shows rendering. http://dx.doi.org/10.1117/12.3028460.2

Table 3. ROIs classified as containing anatomical structures with motion artifacts before registration, i.e. $s_2 > 0$. Listed are image similarity changes (ΔMAD, ΔCC), motion magnitude (d) in µm, and scores based on visual inspection namely (s_1) ROI containing structures with 0: no and 1: yes; (s_2) severity of misalignment before registration ranked as 0: none, 1: little, and 2: large; and (s_3) improvement after registration ranked as -2: much worse, -1: worse, 0: same, 1: better, and 2: much better. Location and anatomy are stated in column Anatomy.

ROI	ΔMAD	ΔCC	d	s_1	s_2	s_3	ΔMAD	ΔCC	d	s_1	s_2	s_3	Anatomy
	Mouse 17 HL 2 phase 1						**Mouse 17 HL 2 phase 15**						
1	-0.04	0.29	12.91	1	2	2	-0.03	0.12	4.97	1	1	1	nasopharynx
2	-0.03	0.19	14.80	1	2	2	-0.03	0.11	3.38	1	1	1	nasopharynx
3	-0.04	0.23	12.01	1	2	2							nasopharynx
7	-0.05	0.39	11.50	1	2	2							anterior skin
13	-0.04	0.25	10.22	1	2	2							nasopharynx
14	-0.04	0.21	10.25	1	2	2							nasopharynx
23	-0.04	0.26	11.02	1	2	2							nasopharynx
24	-0.03	0.18	11.24	1	2	2	-0.03	0.11	3.62	1	1	1	nasopharynx
25	-0.04	0.25	10.63	1	2	1							nasopharynx
26	-0.05	0.32	9.45	1	1	1							anterior skin
27	-0.04	0.23	9.88	1	2	2							nasopharynx
	Mouse 55 HL 1 phase 1						**Mouse 55 HL 1 phase 9**						
1	-0.02	0.08	3.04	1	1	1							air pocket
5	-0.03	0.13	3.59	1	1	0							posterior skin
24	-0.03	0.13	4.21	1	1	0							lateral skin
	Mouse 55 HL 2 phase 1						**Mouse 55 HL 2 phase 10**						
1	-0.04	0.15	4.84	1	1	0							anterior bone
2	-0.03	0.11	5.79	1	1	0							anterior bone
7	-0.03	0.09	4.02	1	1	0							posterior bone
	Mouse 55 HL 4 phase 1						**Mouse 55 HL 4 phase 9**						
2	-0.03	0.06	2.87	1	1	1							posterior bone
3	-0.03	0.14	2.31	1	1	1							anterior bone
4	-0.03	0.19	4.39	1	1	1							nasopharynx
5	-0.03	0.14	2.89	1	1	0							posterior bone
15	-0.03	0.08	4.15	1	1	0							ear
19	-0.03	0.09	5.55	1	1	1							ear
22	-0.03	0.10	4.95	1	1	1							ear
25	-0.03	0.10	4.59	1	1	1							ear
	Mouse 56 HL 1 phase 1						**Mouse 56 HL 1 phase 10**						
13	-0.04	0.14	5.43	1	1	1							anterior border
16	-0.06	0.26	11.01	1	1	0							lateral skin
20	-0.06	0.35	9.17	1	1	1							lateral skin
22	-0.06	0.31	9.51	1	1	1							lateral skin
24	-0.05	0.29	6.54	1	1	1							posterior skin
	Mouse 56 HL 2 phase 1						**Mouse 56 HL 2 phase 10**						
25	-0.03	0.08	5.45	1	1	2							esophagus
	Mouse 56 HL 4 phase 1						**Mouse 56 HL 4 phase 10**						
15	-0.05	0.21	12.48	1	2	1							lateral skin
16	-0.05	0.21	13.06	1	1	0							lateral skin
17	-0.05	0.16	12.41	1	1	2							posterior skin
20	-0.06	0.11	4.87	1	1	1							anterior bone
21	-0.05	0.11	5.24	1	1	1							posterior cable
22	-0.04	0.12	4.98	1	1	1							ear
23	-0.05	0.16	9.80	1	1	2							lateral skin
24	-0.05	0.18	10.57	1	1	1							lateral skin

3.3 Discussion

During the initial registration of the most decorrelated image pairs, we observed that streak artifacts of similar contrast strength were spatially correlated between phase images and thus preventing successful image registration in low-contrast regions. These artifacts were possibly caused by irregularly sampled projections. In future work, we will investigate approaches to retrospectively reduce these effects for the acquired data.

In this study, we changed the strategy to registering the image from a single phase to the mean image of all the other phases. This has the advantage of reducing these artifacts in the mean image. The drawback is that only short movements may be captured, e.g. 10 ms from the left-out phase image to the next one, which is included in the mean image.

We employed retrospective gating because it is more time efficient. However, it leads to more artifacts due to irregularly sampled projections and different angle configurations per phase image. In future acquisitions, we will investigate a prospective gating scheme based on step-scans with fast shutter to avoid radiation overdose and ensure uniform sampling at the same angles for each phase image.[24]

In Mouse 17, the calculated motion magnitudes in the brain were about 10 µm higher than in the other three mice. This could be due to differences in the setup of the *in vivo* experiments (free breathing vs. ventilated, 240 vs. 320 mg Ba/mL contrast agent concentration) or in the acquisition (beamtime B1 vs. B2, 38 vs. 40 keV, 10 vs. 5 ms time between projections, in-house vs. ESRF reconstruction method). The calculated motion magnitudes at the skull and at ventricles with strong contrast were low for all mice, ruling out an issue with global head motion. More flexible registrations, i.e. 16 voxels grid spacing, of the most decorrelated images resulted in similarly high motion magnitudes for the mice with 60'000 projections as for Mouse 17, but not for Mouse 55 with 120'000 projections. Furthermore, we generally extracted larger movements in the imaging plane than in the foot-head direction for all mice. These observations suggest that the spatially correlated artifacts had a greater impact in Mouse 17, as the lower contrast agent concentration only led to weak enhancement of the ventricles. Mouse 17 was also the only specimen measured with free breathing. It is unclear whether this contributed to the increased calculated motion.

During visual inspection, we did not detect any misalignment of the contrast-enhanced ventricles between the most decorrelated phase images prior to image registration. One reason could be insufficient spatial resolution of the acquired images. The expected motion in mice is currently unknown. If we estimate it from the $0.05-0.10$ mm motion measured in humans at the corpus callosum in feet-head direction[25,26] and assume a scaling factor of 14 between human and mouse brain width,[27] we should get $3.6-7.1$ µm motion in mice. As this corresponds to only 0.5 - 1 voxel motion, we plan to acquire local scans with higher image resolution to explore the limits of detecting *in vivo* ventricular motion in mice.

Currently, we usually reconstruct phase images up to 100 ms, since ventricular motion in humans occurs in the first third of the cardiac cycle.[25] To ensure we do not miss this motion in mice, we will reconstruct all possible phase images based on the absolute times from the ECG peak as well as based on times normalized to the duration of the cardiac cycle.

4. CONCLUSIONS

We have developed a method for detecting local displacements of three or more micrometer in 4D *in vivo* X-ray microtromography datasets. While we have not yet detected ventricular motion synchronized with the heartbeat, we have observed and studied limiting factors that may have prevented us from doing so. Furthermore we have developed ideas on how to improve the acquisition and the reconstruction in the future to tackle this challenging problem.

5. ACKNOWLEDGMENTS

We acknowledge the European Synchrotron Radiation Facility (ESRF) for provision of synchrotron radiation facilities under proposal number md1230 and md1324 and we would like to thank Alberto Bravin and Michael Krisch for assistance and support in using beamline ID17. We are grateful for financial support from the Swiss National Science Foundation (Project No. 213535).

REFERENCES

[1] Spector, R., Snodgrass, S. R., and Johanson, C. E., "A balanced view of the cerebrospinal fluid composition and functions: Focus on adult humans," *Experimental Neurology* **273**, 57–68 (2015).

[2] Hladky, S. B. and Barrand, M. A., "The glymphatic hypothesis: the theory and the evidence," *Fluids and Barriers of the CNS* **19**(1), 9 (2022).

[3] de Leon, M. J., Li, Y., Okamura, N., Tsui, W. H., Saint-Louis, L. A., Glodzik, L., Osorio, R. S., Fortea, J., Butler, T., Pirraglia, E., Fossati, S., Kim, H.-J., Carare, R. O., Nedergaard, M., Benveniste, H., and Rusinekothers, H., "Cerebrospinal fluid clearance in Alzheimer disease measured with dynamic PET," *Journal of Nuclear Medicine* **58**(9), 1471–1476 (2017).

[4] ElSankari, S., Balédent, O., Van Pesch, V., Sindic, C., De Broqueville, Q., and Duprez, T., "Concomitant analysis of arterial, venous, and CSF flows using phase-contrast MRI: a quantitative comparison between MS patients and healthy controls," *Journal of Cerebral Blood Flow & Metabolism* **33**(9), 1314–1321 (2013).

[5] Schmid Daners, M., Knobloch, V., Soellinger, M., Boesiger, P., Seifert, B., Guzzella, L., and Kurtcuoglu, V., "Age-specific characteristics and coupling of cerebral arterial inflow and cerebrospinal fluid dynamics," *PLoS One* **7**(5), e37502 (2012).

[6] Liu, P., Owashi, K., Monnier, H., Metanbou, S., Capel, C., and Balédent, O., "Validating the accuracy of real-time phase-contrast MRI and quantifying the effects of free breathing on cerebrospinal fluid dynamics," *Fluids and Barriers of the CNS* **21**(1), 25 (2024).

[7] Li, J., Pei, M., Bo, B., Zhao, X., Cang, J., Fang, F., and Liang, Z., "Whole-brain mapping of mouse CSF flow via HEAP-METRIC phase-contrast MRI," *Magnetic Resonance in Medicine* **87**(6), 2851–2861 (2022).

[8] Badea, C., Hedlund, L., and Johnson, G., "Micro-CT with respiratory and cardiac gating: Micro-CT with respiratory and cardiac gating," *Medical Physics* **31**(12), 3324–3329 (2004).

[9] Fardin, L., Broche, L., Lovric, G., Mittone, A., Stephanov, O., Larsson, A., Bravin, A., and Bayat, S., "Imaging atelectrauma in ventilator-induced lung injury using 4D X-ray microscopy," *Scientific Reports* **11**(1), 4236 (2021).

[10] Klos, A., Bailly, L., Rolland du Roscoat, S., Orgéas, L., Henrich Bernardoni, N., Broche, L., and King, A., "Optimising 4D imaging of fast-oscillating structures using X-ray microtomography with retrospective gating," *Scientific Reports* **14**(1), 20499 (2024).

[11] Schmeltz, M., Ivanovic, A., Schlepütz, C. M., Wimmer, W., Remenschneider, A. K., Caversaccio, M., Stampanoni, M., Anschuetz, L., and Bonnin, A., "The human middle ear in motion: 3D visualization and quantification using dynamic synchrotron-based X-ray imaging," *Communications Biology* **7**(1), 157 (2024).

[12] Decker, Y., Krämer, J., Xin, L., Müller, A., Scheller, A., Fassbender, K., and Proulx, S. T., "Magnetic resonance imaging of cerebrospinal fluid outflow after low-rate lateral ventricle infusion in mice," *JCI Insight* **7**(3) (2022).

[13] Ma, Q., Ries, M., Decker, Y., Müller, A., Riner, C., Bücker, A., Fassbender, K., Detmar, M., and Proulx, S. T., "Rapid lymphatic efflux limits cerebrospinal fluid flow to the brain," *Acta Neuropathologica* **137**, 151–165 (2019).

[14] Girona Alarcón, M., Tanner, C., Humbel, M., Kuo, W., Fardin, L., Bausch, B., Spera, I., Rodgers, G., Deyhle, H., Engelhardt, B., Proulx, S., Müller, B., and Kurtcuoglu, V., "In vivo imaging of central nervous system fluid spaces using synchrotron radiation micro-computed tomography," (2024). submitted.

[15] Bates, J. H. and Smith, B. J., "Ventilator-induced lung injury and lung mechanics," *Annals of Translational Medicine* **6**(19) (2018).

[16] Cavanaugh, D., Johnson, E., Price, R. E., Kurie, J., Travis, E. L., and Cody, D. D., "In vivo respiratory-gated micro-CT imaging in small-animal oncology models," *Molecular Imaging* **3**(1), 15353500200403184 (2004).

[17] Paleo, P., Mirone, A., Nemoz, C., and Vigano, N. R., "ESRF tomography processing software Nabu." https://tomotools.gitlab-pages.esrf.fr/nabu/v2023_2_0.html (2023). [Online; accessed 31-September-2024].

[18] Van Aarle, W., Palenstijn, W. J., Cant, J., Janssens, E., Bleichrodt, F., Dabravolski, A., De Beenhouwer, J., Batenburg, K. J., and Sijbers, J., "Fast and flexible X-ray tomography using the ASTRA toolbox," *Optics Express* **24**(22), 25129–25147 (2016).

[19] Van Aarle, W., Palenstijn, W. J., De Beenhouwer, J., Altantzis, T., Bals, S., Batenburg, K. J., and Sijbers, J., "The ASTRA toolbox: A platform for advanced algorithm development in electron tomography," *Ultramicroscopy* **157**, 35–47 (2015).

[20] Gürsoy, D., De Carlo, F., Xiao, X., and Jacobsen, C., "TomoPy: a framework for the analysis of synchrotron tomographic data," *Journal of Synchrotron Radiation* **21**(5), 1188–1193 (2014).

[21] Pelt, D. M., Gürsoy, D., Palenstijn, W. J., Sijbers, J., De Carlo, F., and Batenburg, K. J., "Integration of TomoPy and the ASTRA toolbox for advanced processing and reconstruction of tomographic synchrotron data," *Journal of Synchrotron Radiation* **23**(3), 842–849 (2016).

[22] Klein, S., Staring, M., Murphy, K., Viergever, M. A., and Pluim, J. P. W., "elastix: A toolbox for intensity-based medical image registration," *IEEE Trans. Med. Imag.* **29**(1), 196–205 (2010).

[23] Shamonin, D., Bron, E., Lelieveldt, B., Smits, M., Klein, S., and Staring, M., "Fast parallel image registration on CPU and GPU for diagnostic classification of Alzheimer's disease," *Frontiers in Neuroinformatics* **7**, 50 (2014).

[24] Shi, Y., Li, J., Li, K., Zhang, X., Chang, P., Huang, Z., Liu, Y., Wang, Y., Zhan, Y., Cao, X., and Zhu, S., "Detector-trigger-based cardiac multiphase micro-CT imaging for small animals," *Journal of X-ray Science and Technology* **31**(5), 1047–1066 (2023).

[25] Kurtcuoglu, V., Soellinger, M., Summers, P., Boomsma, K., Poulikakos, D., Boesiger, P., and Ventikos, Y., "Computational investigation of subject-specific cerebrospinal fluid flow in the third ventricle and aqueduct of sylvius," *Journal of Biomechanics* **40**(6), 1235–1245 (2007).

[26] Almudayni, A., Alharbi, M., Chowdhury, A., Ince, J., Alablani, F., Minhas, J. S., Lecchini-Visintini, A., and Chung, E. M. L., "Magnetic resonance imaging of the pulsing brain: a systematic review," *Magnetic Resonance Materials in Physics, Biology and Medicine* **36**(1), 3–14 (2023).

[27] Pardridge, W. M., "CSF, blood-brain barrier, and brain drug delivery," *Expert Opinion on Drug Delivery* **13**(7), 963–975 (2016).